A dual-templating synthesis strategy to hierarchical ZSM-5 zeolites as efficient catalysts for the methanol-to-hydrocarbons reaction

Journal of Catalysis 361 (2018) 135–142

Contents lists available at ScienceDirect

Journal of Catalysis

journal homepage: www.elsevier.com/locate/jcat

A dual-templating synthesis strategy to hierarchical ZSM-5 zeolites as efficient catalysts for the methanol-to-hydrocarbons reaction

Lingqian Meng [a], Xiaochun Zhu [a,1], Wannaruedee Wannapakdee [a,b], Robert Pestman [a], Maarten G. Goesten [a,2], Lu Gao [a], Arno J.F. van Hoof [a], Emiel J.M. Hensen [a,*]

[a] Inorganic Materials Chemistry, Schuit Institute of Catalysis, Department of Chemical Engineering and Chemistry, Eindhoven University of Technology, P.O. Box 513, 5600 MB Eindhoven, The Netherlands

[b] Department of Chemical and Biomolecular Engineering, School of Energy Science and Engineering, Vidyasirimedhi Institution of Science and Technology, Rayong 21210, Thailand

ARTICLE INFO

Article history:
Received 27 October 2017
Revised 29 December 2017
Accepted 27 February 2018

Keywords:
Hierarchical ZSM-5
Dual-templating synthesis
Methanol-to-hydrocarbons

ABSTRACT

A novel dual-templating synthesis strategy is presented to obtain hierarchical ZSM-5 zeolite using a combination of known structure-directing agents for ZSM-5 synthesis and $C_{16}H_{33}$-[N^+-methylpiperidine] (C_{16}MP) as mesoporogen. C_{16}MP is a cheap surfactant, which can be obtained in a single step by alkylation of N-methylpiperidine. The zeolite materials were extensively characterized for their textural and acidic properties and evaluated on the basis of their ability to convert methanol to hydrocarbons. Bulk and nanosheet (di-quaternary ammonium surfactant) ZSM-5 zeolites served as reference materials. Hierarchical ZSM-5 zeolite can be obtained in this way with diethylamine, n-propylamine, 1,4-diaminobutane, 1,6-diaminohexane. In particular, the combination with diethylamine afforded a material that displayed similar performance in the methanol-to-hydrocarbons reaction as nanosheet ZSM-5. The optimum ZSM-5 zeolite is highly crystalline, contains a large mesopore volume and few silanol groups and external Brønsted acid sites, which contributes to the low rate of deactivation.

1. Introduction

Zeolites are crystalline microporous aluminosilicates, widely used for acid-catalyzed reactions in the chemical industry [1–7]. Strong Brønsted acid sites in zeolites are associated with substitution of Si^{4+} with tetrahedral Al^{3+} in the silica framework [8–12]. ZSM-5 zeolite, a member of pentasil family, is one of the most widely used zeolites in catalysis [6,13]. Its three-dimensional 10-membered ring pore system with ~5.5 Å pores endows ZSM-5 with shape-selective and molecular sieving properties [6]. An inherent disadvantage of the comparable size of the micropores and hydrocarbon reactants with respect to zeolite crystal dimensions is slow mass transport. This can suppress the reaction rate. Moreover, coke formed by side-reactions can rapidly block the pores near the external surface, prematurely deactivating the zeolite catalyst [14–19].

Hierarchical zeolites are materials in which wider pores within or between zeolite crystals are present. The additional pore system enhances diffusion and catalytic performance, while the shape selectivity due to the native micropores is largely preserved [8,9]. There are many ways by which such improved zeolites can be obtained [2,3,8,20]. For instance, alkaline etching is a well-established and economical way to obtain hierarchical MFI zeolite, although it can only be applied to zeolites with a parent Si/Al ratio in the 25–50 range [3,21–23]. It is desirable to synthesize hierarchical zeolites in a single step, for instance by using a structure-directing agent (SDA) that can simultaneously organize silica at the smallest scale into the desired framework topology and at the mesoscale by creating intra- or intercrystalline voids. A general approach is to use amphiphilic surfactants in which the hydrophilic head group serves as the structure-directing moiety, while the hydrophobic tail can for instance limit the crystal growth [6]. An appealing illustration of this approach is to synthesis of ZSM-5 zeolite nanosheets by diquaternary ammonium surfactants developed by Ryoo's group [24]. In these nanosheets, the crystal size is limited to several nanometers in the *b*-direction. These sheets are separated by mesopores. The benefit of nanosheets has been demonstrated for many catalytic reactions. For instance, these materials can reach up to 5 times longer lifetime than their bulk ZSM-5

* Corresponding author.
E-mail address: e.j.m.hensen@tue.nl (E.J.M. Hensen).

[1] Present address: State Key Laboratory of Heavy Oil Processing, The Key Laboratory of Catalysis of CNPC, College of Chemical Engineering, China University of Petroleum, No. 18 Fuxue Road, Changping, Beijing 102249, China.

[2] Present address: Department of Chemistry and Chemical Biology, Cornell University, Baker Lab, 259 East Ave, Ithaca, NY 14850, USA.

https://doi.org/10.1016/j.jcat.2018.02.032
0021-9517/

counterparts in the methanol-to-hydrocarbons (MTH) reaction [15]. The mechanism of formation of nanosheet forms of ZSM-5 has been elucidated recently [25,26]. A drawback of nanosheet synthesis is that it requires expensive diquaternary ammonium surfactants. Thus, it would be appealing to employ cheaper surfactants such as monoquaternary ammonium surfactants [16,19,27–29]. Many of the attempts to combine zeolite-giving SDA with monoquaternary ammonium surfactants have mainly led to formation of mixtures of zeolite and (ordered) mesoporous silica [30,31]. Recently, we have shown that it is possible to use cetyltrimetylammonium as the only SDA to achieve the formation of hierarchical ZSM-5 zeolite in a single step [16]. Although the resulting hierarchical ZSM-5 achieves much better performance than bulk ZSM-5, nanosheet ZSM-5 provides a much longer lifetime [15,16].

Herein, we report a novel dual-templating synthesis of ZSM-5, which yields directly an optimum hierarchical material with similar catalytic performance as ZSM-5 nanosheet synthesized by diquaternary ammonium surfactants. The obtained zeolites were extensively characterized for their morphological, textural and acidic properties by elemental analysis, transmission electron microscopy (TEM), scanning electron microscopy (SEM), X-ray diffraction (XRD), Ar porosimetry, infrared (IR) spectroscopy and solid state nuclear magnetic resonance (NMR) spectroscopy.

2. Experimental

2.1. Synthesis of $C_{16}H_{33}$-[N^+-methylpiperidine] hydroxide

An amount of 0.11 mol of n-methylpiperidine (Aldrich, 98%) and 0.1 mol of 1-bromohexadecane (TCI Europe, >96%) were dissolved in 500 mL of ethanol (Biosolve, 99.9%). The solution was refluxed in an oil bath at 353 K for 24 h. After evaporation of ethanol, the product was filtered, washed with diethyl ether (Biosolve, 99.5%), and dried under evacuation at room temperature for 12 h. The obtained powder was $C_{16}H_{33}$-[N^+-methylpiperidine] bromide (denoted as C_{16}MPBr) [19]. The successful synthesis of C_{16}MPBr was confirmed by ESI-MS and ^{1}H and ^{13}C NMR spectroscopy (Fig. S1). C_{16}MPBr was converted to C_{16}MPOH by dissolution in demi-water and passing the aqueous solution over a column packed with anion exchange resin (Amberlite, IRN-78, OH form).

2.2. Zeolite synthesis

A C_{16}MPOH solution (5 wt%), KOH (Aldrich, 90%), aluminium hydroxide (Aldrich) and diethylamine (DEA, Aldrich, 99.5%) were mixed with demi-water. Afterwards, Ludox AS-40 (Aldrich, 40 wt %) was added to the mixture under vigorous stirring. The final gel had a molar composition of $5C_{16}MP{:}22DEA{:}12K_2O{:}0.95Al_2O_3{:}95SiO_2{:}4000H_2O$. The mixture was transferred to a 45 mL Teflon-lined steel autoclave and heated to 413 K and kept at this temperature for 6 days (rotation, 50 rpm). After crystallization, the white product was filtered, washed with demi-water followed by drying overnight at 383 K. The yield was 54.6%. This zeolite was calcined at 823 K for 10 h under flowing air to remove the surfactant. The calcined zeolite was ion-exchanged three times with 1.0 M NH_4NO_3 solutions followed by calcination at 823 K for 4 h in flowing air to obtain the final proton form. The yield was 75.5%. This zeolite is denoted as MFI(C_{16}MP, DEA). Besides, tetrapropylammonium hydroxide (TPAOH, Merck, 40 wt%), n-propylamine (NPAM, Aldrich, 99%), 1,4-diaminobutane (DAB, Aldrich, 99%), 1,6-diaminohexane (DAH, Aldrich, 98%) were also used as SDA. The synthesis approach was the same as used to obtain MFI (C_{16}MP, DEA), and the resulting materials are denoted as MFI (C_{16}MP, TPA), MFI(C_{16}MP, NPAM), MFI(C_{16}MP, DAB), MFI(C_{16}MP, DAH), respectively. The corresponding yields were 56.0%, 73.8%, 72.1% and 70.0%, respectively.

For comparison, a similar synthesis was performed using ZSM-5 seeds (bulk HZSM-5, Si/Al = 50) instead of the SDA at a SiO_2/seed molar ratio of 19. The obtained product (yield 87.8%) is denoted as MFI(C_{16}MP, Seed). Besides, ZSM-5 nanosheet zeolite (Si/Al = 50 in the gel) was synthesized using $[C_{22}H_{45}{-}N^+(CH_3)_2{-}C_6H_{12}{-}N^+(CH_3)_2{-}C_6H_{13}]Br_2$ as template (MFI-sheet) [15,24].

2.3. Characterization

XRD patterns were recorded on a Bruker D4 Endeavor diffractometer using Cu Kα radiation with a scanning speed of 0.02° s^{-1} in the 2θ range of 5 – 40°.

The elemental composition of the zeolites was determined by ICP-OES (Spectro CirosCCD ICP optical emission spectrometer). For analysis, an equivolumetric mixture of HF (40 wt% in water), HNO_3 (65 wt% in water) and water was used to completely dissolve the zeolites.

Surface area and porosity of zeolites were determined by Ar physisorption in static mode at 87 K on a Micromeritics ASAP 2020 instrument. The zeolites were outgassed at 723 K for 6 h prior to the sorption measurements. The BET surface area of ZSM-5 zeolite was determined in the relative pressure range 0.05–0.25. The total pore volume was calculated at $p/p_0 = 0.97$. The micropore, mesopore volume and pore size distribution (PSD) of zeolites were determined by the NLDFT method (Ar at 87 K assuming slit pores without regularization).

SEM images were taken on a FEI Quanta 200F scanning electron microscope at an accelerating voltage of 3–5 kV. TEM images were taken on a FEI Tecnai 20 at 200 kV. Prior to measurements, the samples were suspended in ethanol and dispersed over a holey Cu grid coated with a carbon film.

IR spectra were recorded in the range of 4000–800 cm^{-1} by a Bruker Vertex V70v instrument with a standard DTGS detector. The spectra were acquired at a 2 cm^{-1} resolution and averaged over 64 scans. Typically, an amount of about 10 mg of zeolite was pressed into thin wafers with a diameter of 13 mm and placed inside a controlled-environment IR transmission cell. Before measurement, the zeolite wafer was firstly heated to 823 K at a rate of 2 K min^{-1} in artificial air. Then, the cell was outgassed at the final temperature until the residual pressure was below 5×10^{-5} mbar. A background IR spectrum was recorded. For CO adsorption, the sample was cooled to 77 K and CO was introduced into the cell via a sample loop connected to a Valco six-port valve. After each dosage, a spectrum was recorded at 77 K. To determine the density of acid sites in zeolites, pyridine and 2,4,6-collidine (2,4,6-trimethylpyridine) was introduced from an ampoule at its vapor pressure for 10 min. Afterwards, the cell was evacuated to a pressure lower than 5×10^{-6} mbar. Further spectra were recorded at 423 K after outgassing for 1 h at 423 K, 573 K and 773 K. In order to quantify the total amount of Brønsted and Lewis acid sites, molar extinction coefficient values of 0.73 cm μmol^{-1} and 1.11 cm μmol^{-1} were applied, respectively [32]. To compute the external Brønsted acid sites, a molar extinction coefficient of 10.1 cm μmol^{-1} of collidine was used [33].

^{27}Al NMR spectra were obtained using a 11.7 Tesla Bruker DMX500 NMR spectrometer operating at 132 MHz. The NMR experiments were performed using a Bruker Triple Channel 2.5 mm MAS probe head spinning at 25 kHz. Saturated $Al(NO_3)_3$ solution were used for ^{27}Al NMR shift calibration.

2.4. Catalytic activity measurements

The zeolites were pelletized and crushed into a 125–250 μm particle size. The powdered catalyst was placed between quartz

wool plugs in a quartz reactor with an internal diameter of 4 mm. Prior to reaction, the catalyst was calcined at 823 K in 20 vol% O_2 in He.

For measuring the constraint index (CI) [34,35], a mixture of n-hexane and 3-methyl pentane (45/55 mol/mol) was passed over the catalyst at 686 K. The feed was obtained by leading a flow of 20 mL min^{-1} of He through a saturator containing n-hexane and 3-methylpentane (Vol/Vol = 1/1) at 264 K. The reactor effluent was analysed online by gas chromatography (Interscience Compact GC equipped with TCD and FID detectors with RT-Q-Bond and Rtx-1 columns). The reaction was carried out for 20 min. The CI was determined by extrapolating the hydrocarbon conversions to zero time via

$$CI = \frac{\log(\text{fraction of n - hexane remaining})}{\log(\text{fraction of 3 - methylpentane remaining})}$$

The MTH reaction was performed at 673 K. Methanol (Merck, 99%) was introduced to the reactor by passing a flow of 30 mL min^{-1} of He through a saturator filled with methanol. The WHSV of methanol was kept at 6 h^{-1}. The reactor effluent was analysed online by gas chromatography (Interscience Compact GC equipped with TCD and FID detectors with RT-Q-Bond and Al_2O_3/KCl columns) [14,15].

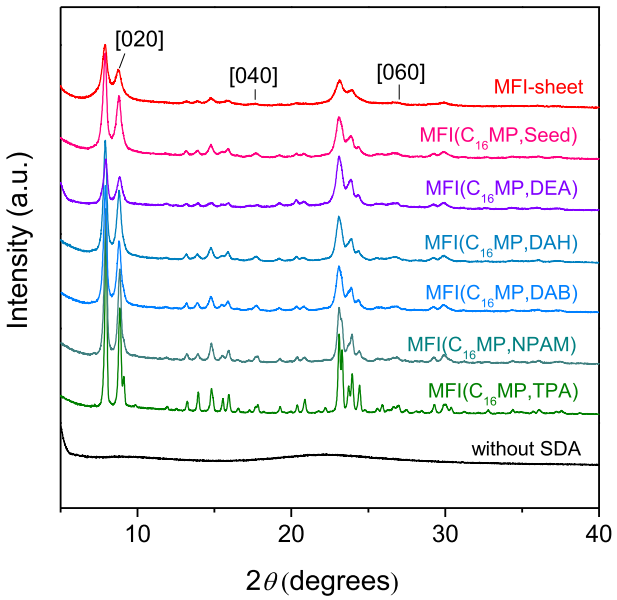

Fig. 1. Powder XRD patterns of the calcined ZSM-5 zeolites.

3. Results and discussion

3.1. Structural characterization

Zeolites were crystallized at 413 K for 6 days under rotation from a gel containing colloidal silica and aluminium hydroxide as silica and alumina sources, the hydroxide form of C_{16}MP as mesoporogen and a variety of small organic cations as SDAs. Fig. 1 shows XRD patterns of zeolites obtained using this dual-templating approach with TPAOH, *N*-propylamine, 1,4-diaminobutane, 1,6-diaminohexane and diethylamine as SDA. In all cases, phase-pure ZSM-5 was obtained with little or no indications of amorphous silica by-product [13]. Peak broadening points to reduced crystal size dimensions, as exemplified by the XRD pattern of MFI-sheet, prepared using a diquaternary ammonium surfactant [15,24], and is also observed for ZSM-5 zeolites obtained by a combination of C_{16}MP with DAB, DAH or DEA. Compared with MFI(C_{16}MP, NPAM) and MFI(C_{16}MP, TPA), the 0k0 reflections were severely broadened suggesting that growth in the *b*-direction of the MFI topology was restricted by C_{16}MP. The main MFI reflections of MFI(C_{16}MP, TPA) are equally sharp as for bulk ZSM-5 zeolite synthesised only with TPA (Fig. S2). In a synthesis with ZSM-5 seeds, the use of C_{16}MP without SDA also yields ZSM-5 exhibiting broadened framework reflections. C_{16}MP clearly facilitates crystallization, as in a comparable synthesis without C_{16}MP mostly amorphous silica was obtained (Fig. S3). Conversely, when only C_{16}MP was used (no SDA and no seeds), amorphous silica was the only product.

Representative SEM and TEM images of the zeolites highlight the different morphologies obtained (Fig. 2). MFI(C_{16}MP, TPA) zeolite consists of large crystalline particles with smooth surfaces. In contrast, the other samples are aggregated particles consisting of zeolite crystals of different size. These primary zeolite crystals are more uniform in shape and size for MFI(C_{16}MP, DAB), MFI (C_{16}MP, DAH) and MFI(C_{16}MP, DEA) than for the other ones. MFI (C_{16}MP, DEA) consists of uniform particles of about 20–30 nm. The morphology of MFI(C_{16}MP, Seed) also consists of such small particles. Clearly, the combination of TPA with C_{16}MP is much less effective in reducing the zeolite crystalline domain size than the other combinations. We have earlier employed C_{16}MP as a mesoporogen in the synthesis of hierarchical SSZ-13 zeolite [19]. In that case, the head group of C_{16}MP will be trapped in the microporous cages of CHA zeolite, as the 8MR (8-membered ring) windows are too small. In contrast, the head group of C_{16}MP can freely move in the 10MR pore channel of ZSM-5 zeolite. Computational modeling showed that repulsion of head group of C_{16}MP with TPA are much larger than with DAH because of the absence of a strong repulsive contribution with neutral amine-based templates [19]. Accordingly, we speculate that the positive charge of TPA results in the repulsion of C_{16}MP from the ZSM-5 pores during zeolite formation. The other templates used in the present study are neutral under the basic synthesis conditions and, accordingly, reduce repulsion so that inclusion of C_{16}MP in the growing zeolite framework becomes possible. The importance of long carbon chains in C_{16}MP molecule for nano-crystals formation is confirmed by the finding that the replacement of C_{16}MP by n-methylpiperidine in the gel with the help of seed resulted only in bulk ZSM-5 zeolite (Fig. S4). In our dual-templating synthesis, the hydrophobic C_{16} tail in C_{16}MP is expected to be partially located in the micropores of the growing zeolite to limit the crystal growth. MFI-sheet has the well-known nanosheet morphology with a uniform thickness of ~3 nm in the *b*-direction (Fig. S5) [15,36].

In Ar physisorption, MFI(C_{16}MP, TPA) presents the typical type I physisorption isotherm (Fig. 3) for microporous solids [37]. The strong Ar uptake at low relative pressure is due to the presence of micropores. The limited uptake at higher pressure implies that the external and mesopore surface area are very low [37,38]. Differently, the isotherms of the other samples are of the IV type with clear H4 hysteresis loops. This is common for porous solids that contain both micropores and mesopores [37]. The hysteresis loop of MFI(C_{16}MP, NPAM) zeolite is less pronounced compared with the other zeolites. The NLDFT method was employed in this work for estimating the pore size distribution (PSD). The characteristic 0.53 nm pore size for ZSM-5 is observed in the PSDs of all of the zeolites. A wide distribution of mesopores in the range 2–10 nm is noted for the MFI(C_{16}MP, NPAM), MFI(C_{16}MP, DAB) and MFI (C_{16}MP, DAH) samples. MFI(C_{16}MP, DEA) contains larger mesopores. Compared with these samples, the much stronger feature in the 2–30 nm range of the PSD for MFI(C_{16}MP, Seed) and MFI-sheet points to a higher mesopore volume. The corresponding textural properties are listed in Table 1. The total pore volume and the mesopore volume of the zeolites follow the sequence: MFI(C_{16}MP,

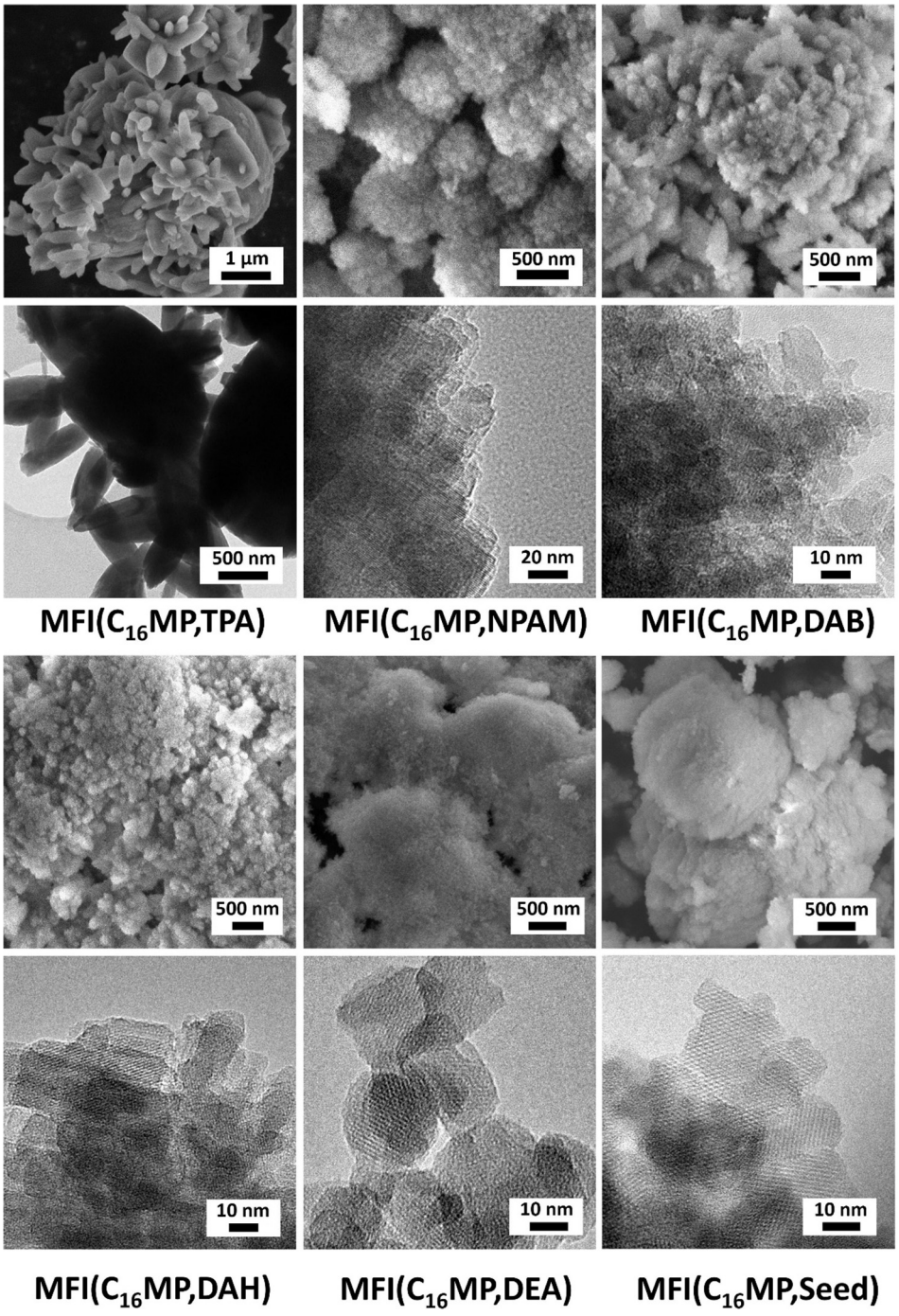

Fig. 2. Representative SEM (top panel) and TEM (bottom panel) images of calcined ZSM-5 zeolites.

TPA) < MFI(C_{16}MP, NPAM) < MFI(C_{16}MP, DAB) < MFI(C_{16}MP, DAH) < MFI(C_{16}MP, DEA) < MFI(C_{16}MP, Seed) < MFI-sheet. MFI-sheet has a much higher mesopore volume (0.68 $cm^3\ g^{-1}$) and BET surface area (567 $cm^2\ g^{-1}$) than the other samples. The micropore volumes of the zeolite samples are comparable. Both the isotherms and PSDs fit the SEM and TEM analysis, supporting the conclusion that the dual-templating strategy yields materials with an intercrystalline mesopore system.

The elemental composition of the zeolites as determined by ICP elemental analysis is listed in Table 1. The Si/Al ratios are between 40 and 50, close to the value in the starting gel. ^{27}Al NMR spectra are given in Fig. 4 and were used to determine the extent of framework introduction of Al (Table 1). Most of the Al atoms are inserted in the zeolite framework, as evident from the strong tetrahedral Al (Al^{IV}) signal at 56 ppm [14,36]. The weak feature at 0 ppm seen in some samples can be ascribed to extraframework Al species in octahedral coordination (Al^{VI}) [14]. Among the hierarchical samples, the fraction of Al^{IV} is lowest for MFI-sheet. This is in line with earlier studies, which reported the difficulties in introducing heteroatoms into the MFI framework during nanosheet formation [15,17]. The value is also relatively low for MFI(C_{16}MP, Seed) zeolite.

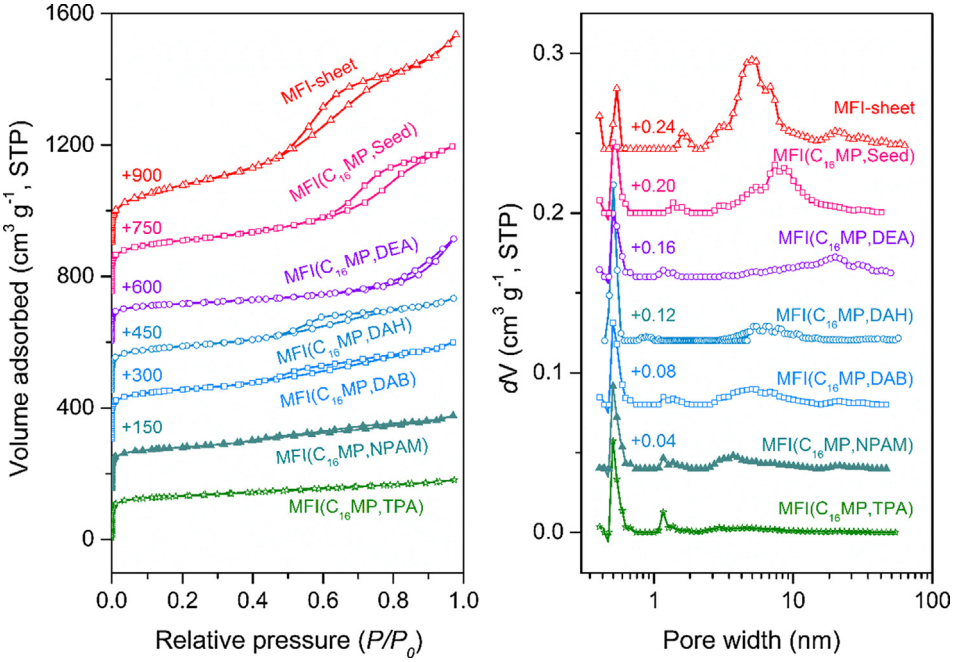

Fig. 3. Ar physisorption isotherms (left) and pore size distribution (PSDs, right) of the calcined ZSM-5 zeolites. The PSDs were calculated with the NLDFT method using the adsorption branch.

Table 1
Si/Al ratio, fraction of framework Al, textural properties, density of acid sites and constraint index values.

Sample	Si/Al[a]	Al_F[b] (%)	S_{BET}[c] ($m^2\ g^{-1}$)	V_{total}[d] ($cm^3\ g^{-1}$)	V_{meso}[e] ($cm^3\ g^{-1}$)	V_{micro}[f] ($cm^3\ g^{-1}$)	[BAS][g] (mmol g^{-1})	[LAS][h] (mmol g^{-1})	$[BAS_{ext}]$[i] (mmol g^{-1})
MFI(C_{16}MP, TPA)	39	95	407	0.23	0.05	0.14	0.33	0.06	<0.01
MFI(C_{16}MP, NPAM)	44	92	409	0.29	0.09	0.12	0.22	0.09	0.04
MFI(C_{16}MP, DAB)	50	92	441	0.35	0.14	0.13	0.24	0.08	0.05
MFI(C_{16}MP, DAH)	50	94	414	0.36	0.17	0.19	0.29	0.07	0.04
MFI(C_{16}MP, DEA)	48	99	368	0.40	0.20	0.11	0.28	0.06	0.03
MFI(C_{16}MP, Seed)	47	88	495	0.57	0.36	0.13	0.23	0.08	0.08
MFI-sheet	47	84	567	0.81	0.68	0.13	0.21	0.12	0.08

[a] Determined using ICP-OES analysis.
[b] Fraction of framework Al determined by ^{27}Al NMR; Al_F (%) = Area of Al_F/(Area of Al_F + Area of Al_{EF}). Area of Al_F determined by integration of ^{27}Al NMR signal between 30 and 100 ppm; Area of Al_{EF} determined by integration of ^{27}Al NMR signal between 30 and −50 ppm.
[c] Brunauer-Emmett-Teller (BET) surface area (p/p_0 = 0.05–0.25).
[d] Total pore volume at p/p_0 = 0.97.
[e] Mesopore volume.
[f] Micropore volume calculated by the NLDFT method using the adsorption branch of the isotherm (Ar at 87 K assuming slit pores without regularization).
[g] Density of Brønsted acid sites (BAS) determined by IR spectra of adsorbed pyridine after evacuation for 1 h at 423 K.
[h] Density of Lewis acid sites (LAS) determined by IR spectra of adsorbed pyridine after evacuation for 1 h at 423 K.
[i] Density of BAS at the external surface determined by IR spectra of adsorbed 2,4,6-collidine after evacuation for 1 h at 423 K.

3.2. Acidity characterization

IR spectroscopy of adsorbed CO at 77 K was employed to determine the acid strength of the ZSM-5 zeolites. The corresponding hydroxyl stretch and the carbonyl stretch regions of the IR spectra are displayed in Fig. 5. The band at 3745 cm^{-1} observed in all spectra with a tail extending to 3700 cm^{-1} is related to silanol groups resonating freely at the external surface (3745 cm^{-1}) or being weakly perturbed inside the micropores at framework defects [39]. Clearly, MFI(C_{16}MP, TPA) contains much less external and internal silanols than the other samples in line with its low external surface area. MFI(C_{16}MP, Seed) and MFI-sheet contain the largest amount of silanols. The other MFI(C_{16}MP, NPAM), MFI (C_{16}MP, DAB) MFI(C_{16}MP, DAH) and MFI(C_{16}MP, DEA) samples contain similar densities of silanols.

All zeolites show a stretching band at 3300 cm^{-1} after CO adsorption, which is characteristic of strongly acidic bridging OH groups perturbed by CO [39–41]. This band is associated with the feature at 3616 cm^{-1} in the spectra of the dehydrated zeolite due to bridging hydroxyl groups. The red shift due to CO adsorption is ~316 cm^{-1} for all zeolites, implying that the Brønsted acid sites in all ZSM-5 zeolites are of similar strength. In the carbonyl stretching region, two bands at 2175 cm^{-1} and 2138 cm-1 belong to CO adsorption on Brønsted acid sites and physisorbed CO, respectively [41]. The shoulder observed at 2158 cm^{-1} observed in some samples is due to CO coordinating to silanols [14,15].

IR spectra of pyridine adsorbed on dehydrated ZSM-5 samples followed by evacuation at 423 K, 573 K and 773 K (Fig. 6, above) were measured to determine the densities of Brønsted and Lewis acid sites. The values obtained after evacuation of pyridine at 423 K are listed in Table 1. Two bands at 1545 cm^{-1} and 1455 cm^{-1} are associated with pyridine adsorbed on Brønsted and Lewis acid sites, respectively [32]. Another band at 1490 cm^{-1} is related to both types of acidity [32]. The BAS density is highest for MFI

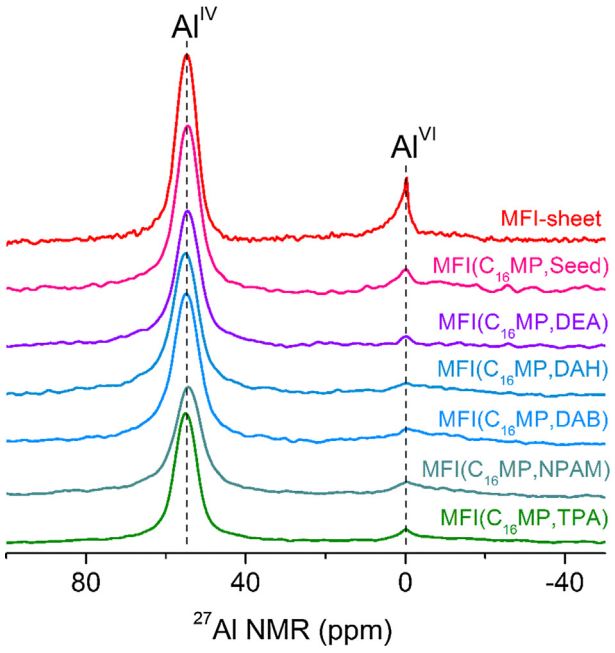

Fig. 4. ^{27}Al MAS NMR spectra of the hydrated HZSM-5 zeolites.

(C_{16}MP, TPA). MFI-sheet possesses much more LAS than the others, in line with the high extraframework Al content determined by ^{27}Al NMR. The densities of Brønsted acid sites on the external zeolite surface (including the mesopore surface) were determined by IR spectroscopy of adsorbed 2,4,6-collidine (Fig. 6, below), and the quantitative data are summarized in Table 1. The peak at 1637 cm^{-1} is correlated with adsorption of 2,4,6-collidine on BAS [33]. As expected, due to the limited mesopore surface area, the concentration of BAS on the external surface of MFI(C_{16}MP, TPA) zeolite is very low. Both MFI(C_{16}MP, Seed) and MFI-sheet zeolites contain a higher concentration of external BAS than the other zeolites, which can be ascribed to their much higher external surface area. Interestingly, despite its high mesopore volume, MFI(C_{16}MP, DEA) zeolite presents a low density of external BAS (0.03 mmol g^{-1}). This suggests that the DEA-C_{16}MP is more conducive to include Al atoms in the bulk of the zeolite relative to the surface in comparison with the diquaternary ammonium surfactant used to obtain nanosheet ZSM-5.

3.3. Catalytic activity measurements

The CI as determined by the relative rates of n-hexane and 3-methylpentane cracking is sensitive to the pore diameter. The results of the CI measurements are collected in Table 2. As all zeolites in the present study have the MFI pore topology, differences in CI are due to the involvement of cracking reactions on the external surface, which does not impose pore restrictions. In line with this, MFI(C_{16}MP, TPA) zeolite shows the highest CI value (2.0), while CI values in the 1.4–1.6 range are found for the mesoporous ZSM-5 samples. The lowest value is observed for zeolite MFI-sheet (1.4), which is the zeolite with the highest external surface area and the highest ratio of the density of external BAS *vs.* total BAS. It can also be seen that the differences in CI for the mesoporous zeolites are relatively small and trend well with the ratio of external and internal BAS.

The catalytic performance of all ZSM-5 zeolites was evaluated in the MTH reaction. Medium-pore zeolites used for methanol conversion processes deactivate due to coke formation [42], which is usually associated with diffusion limitations of heavy products formed in the micropores [39]. The methanol conversion for the ZSM-5 catalysts is displayed in Fig. 7. Details including the product

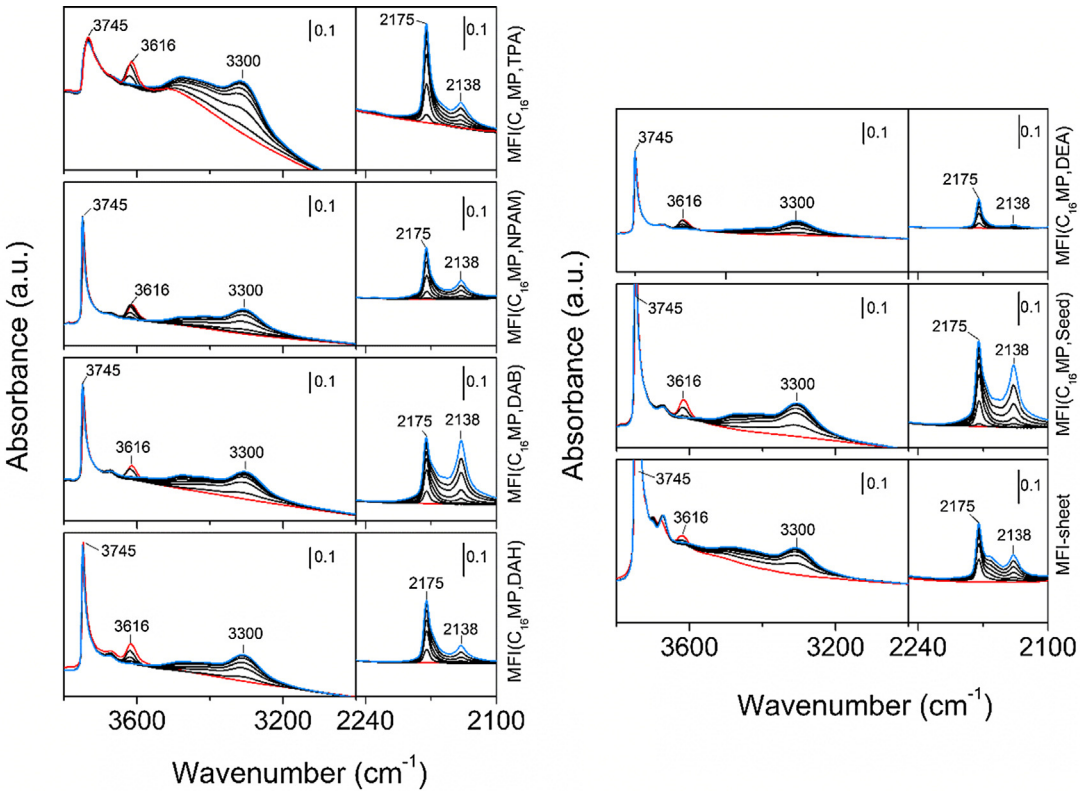

Fig. 5. Hydroxyl (3800 cm^{-1}–3000 cm^{-1}) and carbonyl (2250 cm^{-1}–2100 cm^{-1}) stretch regions of IR spectra for dehydrated calcined ZSM-5 zeolites at 77 K as a function of the CO coverage. The red and blue spectra represent the spectra at the initial and final CO adsorption, respectively. Difference spectra were normalized by weight.

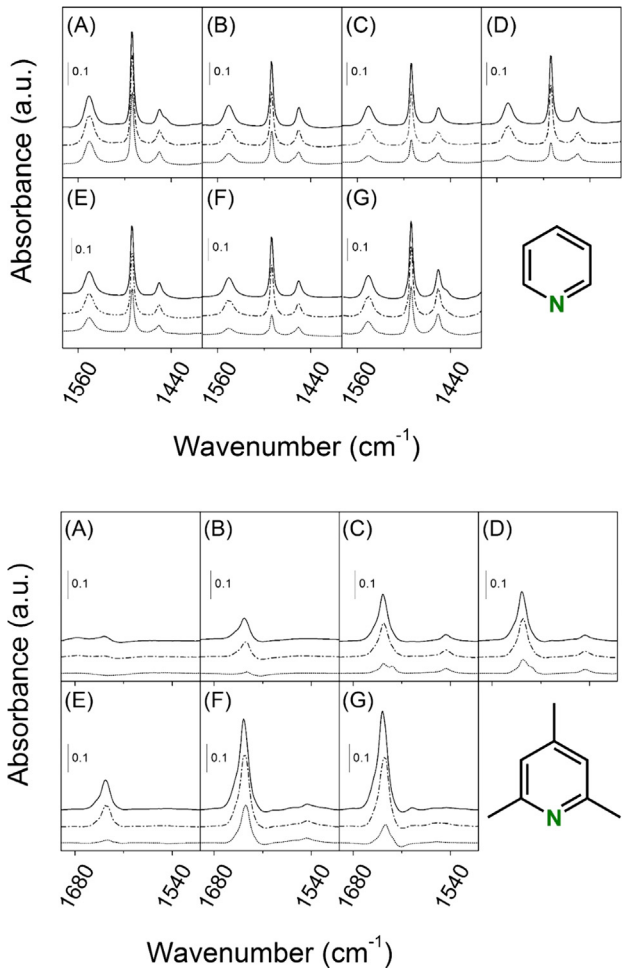

Fig. 6. IR spectra of pyridine and 2,4,6-collidine adsorbed on ZSM-5 zeolites after evacuation at 423 K (solid line), 573 K (dash dot line) and 773 K (dot line). (A) MFI (C_{16}MP, TPA), (B) MFI(C_{16}MP, NPAM), (C) MFI(C_{16}MP, DAB), (D) MFI(C_{16}MP, DAH), (E) MFI(C_{16}MP, DEA), (F) MFI(C_{16}MP, Seed) and (G) MFI-sheet.

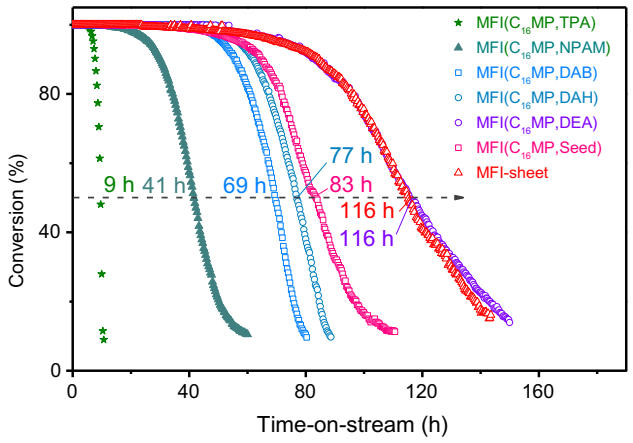

Fig. 7. Methanol conversion of the HZSM-5 zeolites as as a function of time-on-stream. The lifetime of the zeolite catalysts as defined by the time to reach a methanol conversion of 50% is indicated.

distribution after 1 h time on stream are listed in Table 2. Methanol conversion was complete for all the zeolites at the start of the reaction. The lifetime of the zeolites in MTH reaction increases in the order MFI(C_{16}MP, TPA) < MFI(C_{16}MP, NPAM) < MFI(C_{16}MP, DAB) < MFI(C_{16}MP, DAH) < MFI(C_{16}MP, Seed) < MFI-sheet ≈ MFI(C_{16}MP, DEA). As expected, increasing mesoporosity leads to enhanced catalyst lifetime. With the shortest lifetime observed for the bulk MFI (C_{16}MP, TPA) zeolite, the lifetime correlates well with the mesopore volume. Notably, the bulk MFI(C_{16}MP, TPA) sample has a shorter lifetime than a bulk HZSM-5 reference sample prepared without C_{16}MP in the synthesis gel. It is interesting to note that MFI(C_{16}MP, DEA) has a similar long lifetime as the MFI-sheet zeolite, despite its substantially lower mesopore volume. We provide two possible explanations. Concerning coking deactivation, the role of internal and external silanol groups [43] and external BAS has been discussed [39]. According to CO IR, MFI(C_{16}MP, DEA) contains much less internal and external silanol groups than MFI-sheet, which is likely not only due to the larger zeolite crystal domain size for MFI(C_{16}MP, DEA) but also to a higher crystallinity and lower defect density. IR spectra of adsorbed 2,4,6-collidine also show that the external surface of MFI(C_{16}MP, DEA) contains less BAS than MFI-sheet. The coke contents of the spent catalysts (after deactivation) are listed in Table 2. As expected, the coke content is highest for MFI-sheet and it confirms a very effective use of the micropore space. On the other hand, the low coke content in spent MFI(C_{16}MP, DEA) stands out. Accordingly, we speculate that not only a high accessibility of the micropore space due to mesoporosity but also a lower deactivation rate due to the presence of less internal and external silanol groups and a lower external acidity contribute to slower deactivation [39,42,44]. Importantly, the present study shows that a similar optimum performance of nanosheet ZSM-5 in the methanol conversion reaction can be obtained by using a much cheaper template than diquaternary ammonium surfactants.

As typically observed during methanol conversion with ZSM-5 zeolites, the main products are ethylene, propylene and C_{4+} products. Although the exact mechanism of the "hydrocarbon pool" mechanism is very complex, it is usually assumed that the C_{4+} selectivity is a good indicator for the degree of propagation via an olefins-based cycle, while ethylene selectivity can be used for assessing the importance of propagation via polymethylated

Table 2
Constraint index (CI) value, total methanol conversion capacity (TCC, g g^{-1}), product distribution and C_{4+}/ethylene (after 1 h on stream), coke content after deactivation of ZSM-5 zeolite catalysts for the MTH reaction (WHSV = 6 h^{-1}; T = 673 K).

Zeolite	CI	TCC	Selectivity (%)							$C_{4+}/C_2^=$	Coke (%)
			C_1	$C_2^=$	C_2	$C_3^=$	C_3	C_{4+}	Aromatics		
MFI(C_{16}MP, TPA)	2.0	55.6	0.5	10.5	0.7	23.5	3.3	58.2	3.3	5.5	13.1
MFI(C_{16}MP, NPAM)	1.6	250.2	0.9	6.5	<0.1	35.2	2.2	53.1	2.1	8.1	12.5
MFI(C_{16}MP, DAB)	1.6	407.1	0.8	5.5	0.1	25.5	1.7	63.3	3.1	11.5	13.8
MFI(C_{16}MP, DAH)	1.6	452.5	0.3	6.1	0.4	24.5	2.1	64.5	2.2	10.5	17.5
MFI(C_{16}MP, DEA)	1.5	704.3	0.9	5.6	<0.1	35.4	1.9	53.7	2.4	9.5	11.9
MFI(C_{16}MP, Seed)	1.5	500.3	1.3	6.6	0.1	31.9	2.1	53.7	4.5	8.1	13.1
MFI-sheet	1.4	685.6	0.2	2.6	<0.1	41.5	2.0	52.0	1.8	20.0	18.5
Bulk ZSM-5[a]	n.d.[b]	122.7	0.4	9.3	0.1	30.2	4.4	52.4	3.2	5.6	10.1

[a] Conventional bulk ZSM-5 zeolite synthesized by TPAOH [15].
[b] Not determined.

benzene intermediates [15,45]. A salient detail noted from the data in Table 2 is that the C_{4+}/ethylene ratio of MFI(C_{16}MP, TPA) zeolite (5.5) is much lower than for the other zeolites with strongly reduced crystal domain size. On contrary, MFI-sheet displays the highest C_{4+}/ethylene ratio of 20. Thus, the olefins-based cycle becomes more important with increasing mesoporosity. We tentatively ascribe this to a shorter intracrystalline residence time of polymethylated benzenes with decreasing crystalline domain size, thereby suppressing the aromatics-based cycle that results in ethylene. Clearly, the MFI-sheet zeolite stands out on the basis of this criterion, consistent with the extremely thin intracrystalline diffusion lengths compared to the other zeolites. On this basis, we can add further support for the speculation that a lower defect and external BAS density explains the good catalytic performance of MFI(C_{16}MP, DEA).

The total methanol conversion capacity (TCC) of these zeolites was determined according to the method proposed by Bjørgen et al. (Fig. S6) [46]. The corresponding data are given in Table 2. The TCC is lowest for MFI(C_{16}MP, TPA), increases with mesoporosity and is highest for MFI(C_{16}MP,DEA) and MFI-sheet. Notably, MFI (C_{16}MP, DEA) can convert up to five times more methanol than a conventional bulk ZSM-5 zeolite under the same reaction conditions.

4. Conclusions

A dual-templating synthesis strategy was developed to hydrothermally synthesize hierarchical ZSM-5 zeolites. By combination of the mono-quaternary ammonium surfactant (C_{16}MP) and DEA, a hierarchical ZSM-5 zeolite can be obtained that exhibits comparable catalytic performance in the MTH reaction as ZSM-5 nanosheet zeolite synthesized by an expensive di-quaternary ammonium surfactant. The new hierarchical zeolite is highly mesoporous and crystalline with a low amount of silanol and external Brønsted acid sites. Instead of DEA, NPAM, DAB and DAH can also be used to obtain hierarchical ZSM-5. When TPA is used as the SDA, bulk ZSM-5 zeolite is obtained which indicates that strong electrostatic repulsive interactions between trapped TPA and the head group of C_{16}MP expel the latter from the growing zeolite. Accordingly, it can be speculated that the use of a non-charged SDA is essential to our approach. While the MTH performance of the new optimum material is similar to that of ZSM-5 nanosheet zeolite, the kinetics reveal that the increased lifetime of the sample obtained by a combination of C_{16}MP and DEA is not only due to a more effective use of the micropore space but also to a lower density of internal defect and external silanol sites and external Brønsted acid sites. The dual-templating synthesis of hierarchical zeolites by combining a mesoporogen with different structure directing agents forms a new strategy to obtain hierarchical zeolites.

Acknowledgement

LM acknowledges financial support from the China Scholarship Council. EJMH thanks the Netherlands Organization for Scientific Research (TOP grant and NWO-India grant). TEM measurements were done in the Cryo-TEM Research Unit of Eindhoven University of Technology.

Appendix A. Supplementary material

Supplementary data associated with this article can be found, in the online version, at https://doi.org/10.1016/j.jcat.2018.02.032.

References

[1] C.S. Cundy, P.A. Cox, Chem. Rev. 103 (2003) 663–702.
[2] M. Hartmann, A.G. Machoke, W. Schwieger, Chem. Soc. Rev. 45 (2016) 3313–3330.
[3] D. Verboekend, J. Pérez-Ramírez, Catal. Sci. Technol. 1 (2011) 879–890.
[4] J. Pérez-Ramírez, C.H. Christensen, K. Egeblad, C.H. Christensen, J.C. Groen, Chem. Soc. Rev. 37 (2008) 2530–2542.
[5] K. Moller, T. Bein, Chem. Soc. Rev. 42 (2013) 3689–3707.
[6] T. Prasomsri, W. Jiao, S.Z. Weng, J. Garcia Martinez, Chem. Commun. 51 (2015) 8900–8911.
[7] M.E. Davis, Nature 417 (2002) 813–821.
[8] V. Valtchev, L. Tosheva, Chem. Rev. 113 (2013) 6734–6760.
[9] K. Li, J. Valla, J. Garcia-Martinez, ChemCatChem 6 (2014) 46–66.
[10] K. Na, M. Choi, R. Ryoo, Microporous Mesoporous Mater. 166 (2013) 3–19.
[11] S. Mitchell, A.B. Pinar, J. Kenvin, P. Crivelli, J. Kärger, J. Pérez-Ramírez, Nat. Commun. 6 (2015) 8633–8645.
[12] W.J. Roth, P. Nachtigall, R.E. Morris, J. Čejka, Chem. Rev. 114 (2014) 4807–4837.
[13] D.H. Olson, G.T. Kokotailo, S.L. Lawton, W.M. Meier, J. Phys. Chem. 85 (1981) 2238–2243.
[14] X. Zhu, L. Wu, P.C.M.M. Magusin, B. Mezari, E.J.M. Hensen, J. Catal. 327 (2015) 10–21.
[15] L. Meng, X. Zhu, B. Mezari, R. Pestman, W. Wannpakdee, E.J.M. Hensen, ChemCatChem 9 (2017) 3942–3954.
[16] L. Meng, B. Mezari, M.G. Goesten, E.J.M. Hensen, Chem. Mater. 29 (2017) 4091–4096.
[17] L. Meng, X. Zhu, E.J.M. Hensen, ACS Catal. 7 (2017) 2709–2719.
[18] L. Wu, V. Degirmenci, P.C.M.M. Magusin, B.M. Szyja, E.J.M. Hensen, Chem. Commun. 48 (2012) 9492–9494.
[19] X. Zhu, R. Rohling, G. Filonenko, B. Mezari, J.P. Hofmann, S. Asahina, E.J.M. Hensen, Chem. Commun. 50 (2014) 14658–14661.
[20] Q.L. Wang, G. Giannetto, M. Torrealba, G. Perot, C. Kappenstein, M. Guisnet, J. Catal. 130 (1991) 459–470.
[21] D. Verboekend, S. Mitchell, M. Milina, J.C. Groen, J. Pérez-Ramírez, J. Phys. Chem. C 115 (2011) 14193–14203.
[22] J.C. Groen, J.C. Jansen, J.A. Moulijn, J. Pérez-Ramírez, J. Phys. Chem. B 108 (2004) 13062–13065.
[23] J.C. Groen, L.A.A. Peffer, J.A. Moulijn, J. Pérez-Ramírez, Chem. Eur. J. 11 (2005) 4983–4994.
[24] M. Choi, K. Na, J. Kim, Y. Sakamoto, O. Terasaki, R. Ryoo, Nature 461 (2009) 246–249.
[25] X. Zhu, M.G. Goesten, A.J.J. Koekkoek, B. Mezari, N. Kosinov, G. Filonenko, H. Friedrich, R. Rohling, B.M. Szyja, J. Gascon, F. Kapteijn, E.J.M. Hensen, Chem. Sci. 7 (2016) 6506–6513.
[26] M.G. Goesten, X. Zhu, B. Mezari, E.J.M. Hensen, Angew. Chem. Int. Ed. 56 (2017) 5160–5163.
[27] Z. Wang, C. Li, H.J. Cho, S.-C. Kung, M.A. Snyder, W. Fan, J. Mater. Chem. 3 (2015) 1298–1305.
[28] X. Zhou, H. Chen, Y. Zhu, Y. Song, Y. Chen, Y. Wang, Y. Gong, G. Zhang, Z. Shu, X. Cui, J. Zhao, J. Shi, Chem. Eur. J. 19 (2013) 10017–10023.
[29] M. Liu, J. Li, W. Jia, M. Qin, Y. Wang, K. Tong, H. Chen, Z. Zhu, RSC Adv. 5 (2015) 9237–9240.
[30] A. Karlsson, M. Stöcker, R. Schmidt, Microporous Mesoporous Mater. 27 (1999) 181–192.
[31] L. Huang, W. Guo, P. Deng, Z. Xue, Q. Li, J. Phys. Chem. B 104 (2000) 2817–2823.
[32] J. Datka, A.M. Turek, J.M. Jehng, I.E. Wachs, J. Catal. 135 (1992) 186–199.
[33] N.S. Nesterenko, F. Thibault-Starzyk, V. Montouillíout, V.V. Yushchenko, C. Fernandez, J.-P. Gilson, F. Fajula, I.I. Ivanova, Kinet. Catal. 47 (2006) 40–48.
[34] V.J. Frillette, W.O. Haag, R.M. Lago, J. Catal. 67 (1981) 218–222.
[35] J.R. Carpenter, S. Yeh, S.I. Zones, M.E. Davis, J. Catal. 269 (2010) 64–70.
[36] L. Wu, P.C.M.M. Magusin, V. Degirmenci, M. Li, S.M.T. Almutairi, X. Zhu, B. Mezari, E.J.M. Hensen, Microporous Mesoporous Mater. 189 (2014) 144–157.
[37] M. Thommes, Chem. Ing. Tech. 82 (2010) 1059–1073.
[38] K.S.W. Sing, R.T. Williams, Adsorpt. Sci. Technol. 22 (2004) 773–782.
[39] U. Olsbye, S. Svelle, M. Bjørgen, P. Beato, T.V.W. Janssens, F. Joensen, S. Bordiga, K.P. Lillerud, Angew. Chem. Int. Ed. 51 (2012) 5810–5831.
[40] M.S. Holm, S. Svelle, F. Joensen, P. Beato, C.H. Christensen, S. Bordiga, M. Bjorgen, Appl. Catal., A 356 (2009) 23–30.
[41] S.M.T. Almutairi, B. Mezari, E.A. Pidko, P.C.M.M. Magusin, E.J.M. Hensen, J. Catal. 307 (2013) 194–203.
[42] D. Mores, J. Kornatowski, U. Olsbye, B.M. Weckhuysen, Chem. Eur. J. 17 (2011) 2874–2884.
[43] P. Sazama, B. Wichterlova, J. Dedecek, Z. Tvaruzkova, Z. Musilova, L. Palumbo, S. Sklenak, O. Gonsiorova, Microporous Mesoporous Mater. 143 (2011) 87–96.
[44] J. Kim, M. Choi, R. Ryoo, J. Catal. 269 (2010) 219–228.
[45] Z. Liu, X. Dong, Y. Zhu, A.-H. Emwas, D. Zhang, Q. Tian, Y. Han, ACS Catal. 5 (2015) 5837–5845.
[46] M. Bjørgen, F. Joensen, M. Spangsberg Holm, U. Olsbye, K.-P. Lillerud, S. Svelle, Appl. Catal., A 345 (2008) 43–50.